



## Stochastic strong-ground motion simulation in the Santiago metropolitan region considering an Mw 7.8 intraplate intermediate-depth earthquake

Christian Flores <sup>a,b,\*</sup>, Javier Ojeda <sup>a,d</sup>, Cristian Otarola <sup>a</sup>, Sebastian Arriola <sup>c</sup>, Sergio Ruiz <sup>a</sup>

<sup>a</sup> Departamento de Geofísica, Universidad de Chile, Santiago, Chile

<sup>b</sup> Departamento de Geología, Universidad de Chile, Santiago, Chile

<sup>c</sup> Centro Sismológico Nacional, Universidad de Chile, Santiago, Chile

<sup>d</sup> Université Paris Cité, Institut de Physique du Globe de Paris, CNRS, Paris, France

### ARTICLE INFO

**Keywords:**

Strong-ground motion simulation

Stochastic high-frequency method

Santiago, Chile

Intraplate intermediate-depth event

### ABSTRACT

Large intraplate intermediate-depth (IID) events are the most destructive to Chilean structures and they occurred throughout the country. Cities located above the hypocenters of these large earthquakes have been completely destroyed. In recent years, only small- and moderate-magnitude IID events have been reported below Santiago, the most populated Chilean city; however, the occurrence of large-magnitude IID events cannot be ruled out. In this study, we investigated the strong-ground motion generated by large-magnitude earthquakes occurring below the Santiago metropolitan region. We used a stochastic methodology to simulate synthetic records, considering IID events of magnitude Mw 7.8. To validate this method, we simulated intermediate-depth events of magnitudes Mw ~5–6 that occurred near Santiago. We further calibrate our results by reproducing the strong-ground motion data recorded during the 2005 Tarapacá Mw 7.8 Northern Chile IID earthquake. We observe that in some areas of the Santiago Basin, high PGA values can reach values close to 1 g, in which, in addition to directivity effects and takeoff angles, the rupture distances (~100 km) and soil type (C) play a key role in amplifying strong-ground motion. Finally, our findings highlight the importance of reproducing high-frequency time histories as a proxy to re-evaluate the seismic hazard due to large IID earthquakes.

### 1. Introduction

Moderate- and large-magnitude intraplate intermediate-depth (IID) events frequently occur throughout the territory of Chile (e.g., Herrera et al., 2017, 2023; Ruiz et al., 2019; Delouis and Legrand, 2007; Peyrat et al., 2006). The most destructive events of the last century were in Chillán (1939), Calama (1950), and Tarapacá (2005) of magnitudes around M 8.0 (Beck et al., 1998; Ruiz and Madariaga, 2018). Before the 20th century, few intraplate events were recorded by historians and seismologists, probably because many were poorly recorded in the seismic catalogs built during the 1970s (Ruiz and Madariaga, 2018). The main exception is the 1647 earthquake, which caused extensive damage in the Santiago metropolitan area and has recently been reanalyzed, with a proposed origin approximately 100 km deep within the Nazca Plate (Udfas et al., 2012; Cisternas et al., 2012). In addition to the diffused historical knowledge of these events, the physical mechanism of enigmatic rupture prevents the correct estimation of potential seismic hazards (Magott et al., 2016; Houston, 2015; Chen et al., 2014; Green and Houston, 1995).

The Santiago Basin, located in Central Chile, is characterized by different types of soil (Leyton et al., 2011; Yáñez et al., 2015; González et al., 2018; Salomón et al., 2021), from clay to gravel deposits that present a diversity of dynamic amplification levels (Bonnefoy-Claudet et al., 2009; Pastén et al., 2016) and a variety of strong-ground motions (Bustos et al., 2023). The main strong-ground motion simulation for Santiago Basin was performed using 2D numerical simulations considering hypothetical earthquake ruptures along the San Ramon Fault (Pilz et al., 2011; Bustos et al., 2023), which is the most important shallow tectonic feature of the western Andes Cordillera (Vargas et al., 2014; Ammirati et al., 2019, 2022). Bustos et al. (2023) showed the relevance of the type of soil and basin geometry in amplifying strong-ground motion caused by an earthquake. However, no large earthquakes have been recorded beneath Santiago. In Chile, the only large-magnitude IID earthquake well recorded by accelerometers was the 2005 Tarapacá Mw 7.8 earthquake in Northern Chile, where the maximum acceleration reached a value close to 0.7 g (Delouis and Legrand, 2007; Peyrat et al., 2006).

\* Corresponding author at: Departamento de Geofísica, Universidad de Chile, Santiago, Chile.

E-mail addresses: [edden.c.f.g@gmail.com](mailto:edden.c.f.g@gmail.com) (C. Flores), [jojeda@dgf.uchile.cl](mailto:jojeda@dgf.uchile.cl) (J. Ojeda), [crotarola@ug.uchile.cl](mailto:crotarola@ug.uchile.cl) (C. Otarola), [sarriola@csn.uchile.cl](mailto:sarriola@csn.uchile.cl) (S. Arriola), [sruiz@uchile.cl](mailto:sruiz@uchile.cl) (S. Ruiz).

In this study, we considered a stochastic methodology that allows us to simulate the strong-ground motion of potential large-magnitude IID earthquakes. Our simulations were first calibrated with different IID earthquakes that occurred close to Santiago and were recorded well by the strong-ground motion instruments of the Centro Sismológico Nacional (CSN, Barrientos, 2018; Leyton et al., 2018a). The average magnitude of these events was approximately M ~5.1; therefore, we also simulated the 2005 Tarapacá earthquake (Peyrat et al., 2006; Delouis and Legrand, 2007). Finally, considering the different soil conditions, we simulated hypothetical IID events Mw 7.8 below Santiago. Our results show the applicability of high-frequency strong-ground motion simulations that can be considered for a better understanding of the seismic hazard in Central Chile and for re-evaluating the potential risk of large intermediate-depth earthquakes below high-density cities, such as Santiago.

## 2. Methodology

Stochastic strong-ground motion simulations were initially proposed by Boore (1983) as a fast and reliable method for capturing high-frequency content radiated by earthquakes. Since then, different researchers have improved the methodology (e.g., Beresnev and Atkinson, 1997; Boore, 2003; Motazedian and Atkinson, 2005; Otarola and Ruiz, 2016; Ruiz et al., 2018; Ojeda et al., 2021) by incorporating different sources, paths, and sites effects to calculate synthetic accelerograms and contrasting them with the observed records. Strong-ground motion simulations initially considered only vertical incident waves from a point fault source. Currently, P, SV, and SH waves associated with a finite fault of any event can be simulated to generate three-component strong-ground motion synthetic records (e.g., Ruiz et al., 2018; Ojeda et al., 2021).

It is well known that the ground shaking of basins is usually well simulated in the low-frequency range using numerical approaches (e.g., finite difference and spectral element methods); on the contrary, high-frequency stochastic methods usually do not reproduce long-period ground motions in basins (see details in Douglas and Aochi, 2008). Although it is challenging to model the low-frequency content using stochastic methods, the most important contribution in the strong-ground motion produced by IID events originates from their characteristic high-frequency content. In addition, we use a stochastic method that incorporates heterogeneities in the source and trajectory effects (calculating the takeoff angle, travel time, and trajectory sub-fault/station) and an acceptable estimate of the site effect with the use of generic rock soil amplification (GRSA) that is related to Vs30.

The methodology applied here is the same as that proposed by Otarola and Ruiz (2016), Ruiz et al. (2018), and Ojeda et al. (2021), and it has two main parts to model high-frequency ground motion simulations, which are briefly described in the following subsection.

### 2.1. Simulation of P, SV, and SH waves at the surface or hard rock

We simulated the P, SV, and SH waves to reproduce high-frequency accelerograms in both horizontal and vertical components. Fig. 1 shows the main steps proposed by Otarola and Ruiz (2016) and Ruiz et al. (2018). Based on the idea that higher frequencies exhibit random behavior, we used random white noise traces for P, SV, and SH waves (Fig. 1a). The white noise records for each component were modulated with an envelope proposed by Saragoni and Hart (1973), where the duration and amplitude of the records are as a function of the  $T_{gm}$ ,  $\eta$  and  $\epsilon$  constants (see details in Boore, 2003). The same time-window envelope is considered for P, SV, and SH waves, although they should vary slightly (Fig. 1b). We then calculated the Fourier transform for each randomly modulated white-noise trace (Fig. 1c). In the frequency domain (Fig. 1d), we convolved each trace with the function  $A_{ijm}^X$  (Eq. (1)), in which the superscript X corresponds to P, SV, or SH waves,

the subscripts i and j indicate subfault positions, and the subscript m indicates the simulated station.

$$A_{ijm}^X = \frac{\langle R \rangle_{ijm}^X F S_{ijm}^X E P_{ijm}^X M_{0ij}}{4\pi\rho V_X^3} \frac{(2\pi f)^2}{1 + \left(\frac{f}{f_{cij}^X}\right)^r} G(R_{ijm}) \\ \times \exp\left(-\frac{\pi f R_{ijm}}{Q_X(f)V_X}\right) Amp(f) \exp(-\pi\kappa_{0m}f) \quad (1)$$

Eq. (1) considers the Brune spectrum (Brune, 1970) to model the source effect. However, we also took into account other aspects apart from the sources, paths, and site effects such as energy partition (EP), free surface (FS), radiation pattern effects ( $\langle R \rangle$ , Aki and Richards, 2002), geometric spreading ( $G(R)$ ), and the general amplification function ( $Amp$ ), together with the parameters of seismic moment ( $M_0$ ), frequency ( $f$ ), corner frequency ( $f_c$ ), quality factor ( $Q(f)$ ), seismic wave velocity ( $V_X$ , where X can be P or S), and density ( $\rho$ ). Further details on the effects of these parameters can be found in Ruiz et al. (2018).

We applied an inverse Fourier transform to return each modeled accelerogram from the frequency domain to the time domain (Fig. 1e). The three-component accelerograms in the NS, EW, and Z coordinate systems were obtained using the azimuthal angles for each pair of sub-fault/station and by rotating the radial, tangential, and upward coordinate systems (Fig. 1f). The accelerograms obtained in each sub-fault/station have a time lag calculated by the ray path in the regional velocity model (Fig. 1i). The modeled accelerograms for each sub-fault were summed to obtain the records in the NS, EW, and Z components (Fig. 1g). Finally, the synthetic records were compared to the observed records (Fig. 1h).

### 2.2. Simulation on the surface hard rock or soil

These records were simulated by considering two different surface conditions. On the one hand, if the records are simulated under hard rock conditions, the simulation stops at the step indicated in Fig. 1g by considering an amplification factor  $Amp(f) = 1$  (Eq. (1)), namely, discarding amplifications due to site effects. However, if the records were simulated on soil conditions, we considered generic rock soil amplification (GRSA) using the soil classification defined in Ojeda et al. (2021) and the references therein.

These GRSA curves correspond to the soil classification NTC-18 code based on Boore and Joyner (1997). Different studies (Boore and Joyner, 1997; Wills et al., 2000; Boore, 2004; Boore et al., 2011) conducted in different parts of the world have tested the relationship of the amplification factor due to the site effect with the characteristics and properties of the shallow section of the soil, more specifically, with the average velocity of Vs up to 30 m deep at the point of observation (i.e., the station). The degree of excitation or amplification of the ground motion increased, whereas the velocity values Vs decreased. Soil type classification was determined by the values of Vs30: type A for  $Vs30 > 750$ , type B for  $360 < Vs30 < 750$ , and type C for  $Vs30 < 360$ . The Vs30 values were estimated from the velocity profiles of the CSN following the VSz30 methodology proposed by Boore (2004) for each station placed in the Santiago metropolitan region. We also used the Vs30 values proposed by Pozo et al. (2023), specifically for stations MT02 and MT05. For stations without Vs30 or VSz30 information, we chose the soil class that best fit the observed and synthetic records of each site (Table 2).

The GRSA curves allowed us to better characterize the soil amplification factors under conditions such as those in the Santiago metropolitan region, where we found drawbacks in obtaining exact amplification models from the local velocity structures below each station (Leyton et al., 2018a,b). We studied the performance of our simulations by considering the GRSA curves in the time and frequency domains (Fig. 1j and k, respectively).

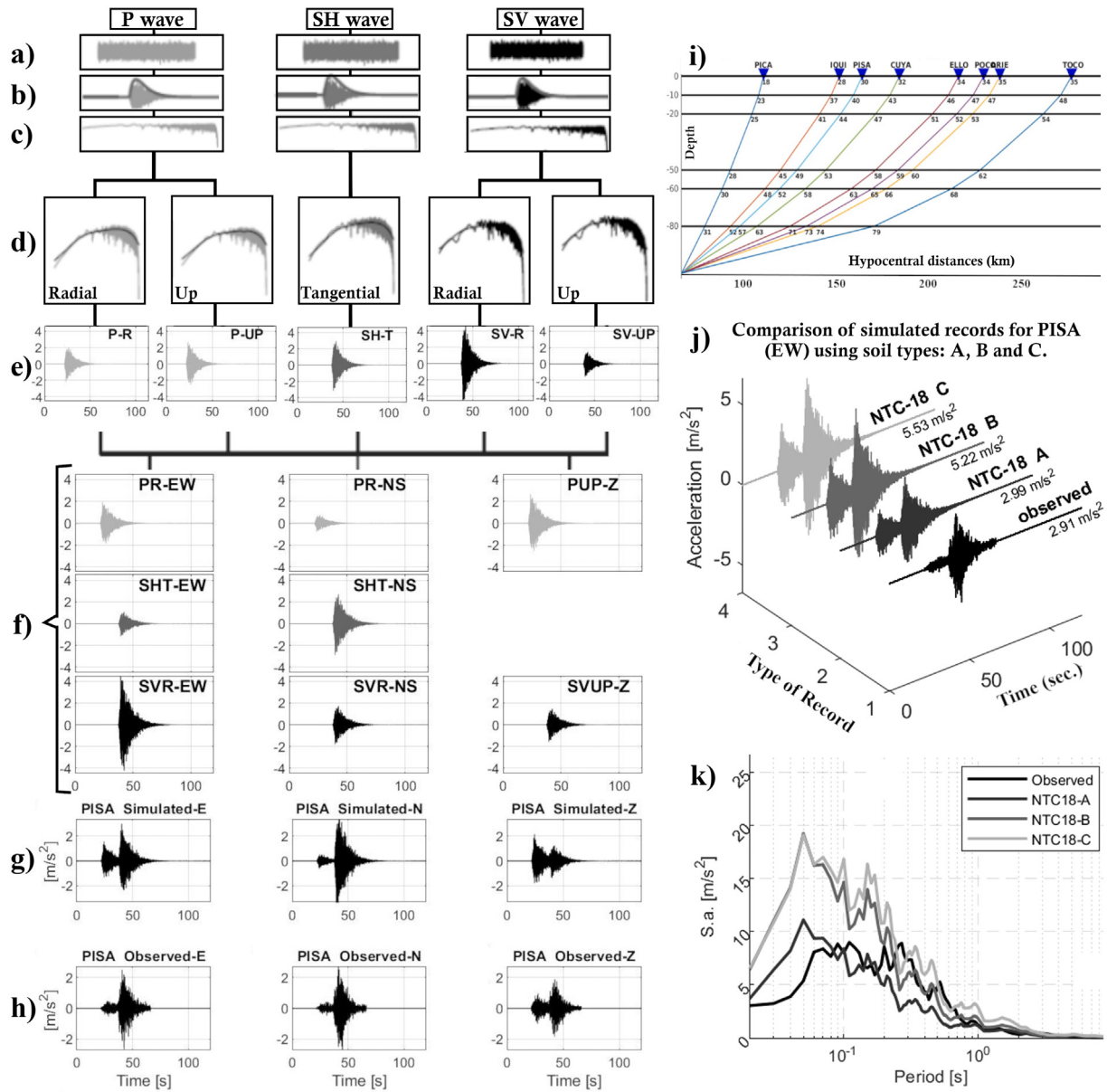


**Fig. 1.** Diagram of the finite-fault stochastic simulation method. (a) Random white noise. (b) Modulated white noise in time. (c) Modulated white noise in the frequency domain. (d) Normalized modulated white noise for Brune spectra and convolved with the equation (1). (e) Time series from radial and tangential waves from modulated white noise. (f) Time series rotated in EW, NS, and Z components. (g) Simulated records, and (h) Observed records for the PISA station (simulation and observation from the 2005 Tarapacá earthquake). (i) Profile view of wave trajectory from one sub-sources to all the stations. (j) Different simulations on soil using different soil types A, B, and C. (k) Comparison of the spectra of (j) and the observed record for the PISA station that recorded the Tarapacá earthquake.

### 3. Strong-ground motion data and seismic source parameters

#### 3.1. Santiago metropolitan region strong-ground motion data

We considered the IID events with a magnitude between Mw 4.5–5.7, within the period 2015–2021. These events have an epicenter location less than 100 km from downtown Santiago, and we selected only the events with a minimum of twenty strong-ground motion records in the Santiago Basin. We used stations fully deployed by the CSN (Barrientos, 2018; Leyton et al., 2018a), where at least 14 stations were located in the metropolitan region with different soil types. The selected events are presented in Table 1 and Fig. 2. Table 2 lists the coordinates and soil types of the 23 strong-ground motion stations considered in this study.

#### 3.2. Building an earthquake scenario based on the 2005 Tarapacá Mw 7.8 earthquake

The Santiago metropolitan region did not experience a large IID earthquake of  $M > 7$ . However, this is different along other areas of the Chilean subduction zone, where recent moderate and large IID earthquakes have been well recorded by modern instrumentation. The event that met these criteria was the 2005 Tarapacá Mw 7.8 earthquake. Fig. 3 shows the strong-ground motion recorded during this event, in which large PGA values were obtained ( $\sim 0.7$  g). The stochastic simulation of this Mw 7.8 earthquake is important because it allows us to extrapolate our simulations from moderate- to large-magnitude earthquakes. We used the same parameters considered for the simulation of a moderate earthquake (Mw~5–6) to simulate this major event; however, instead of considering a fault point, we used the

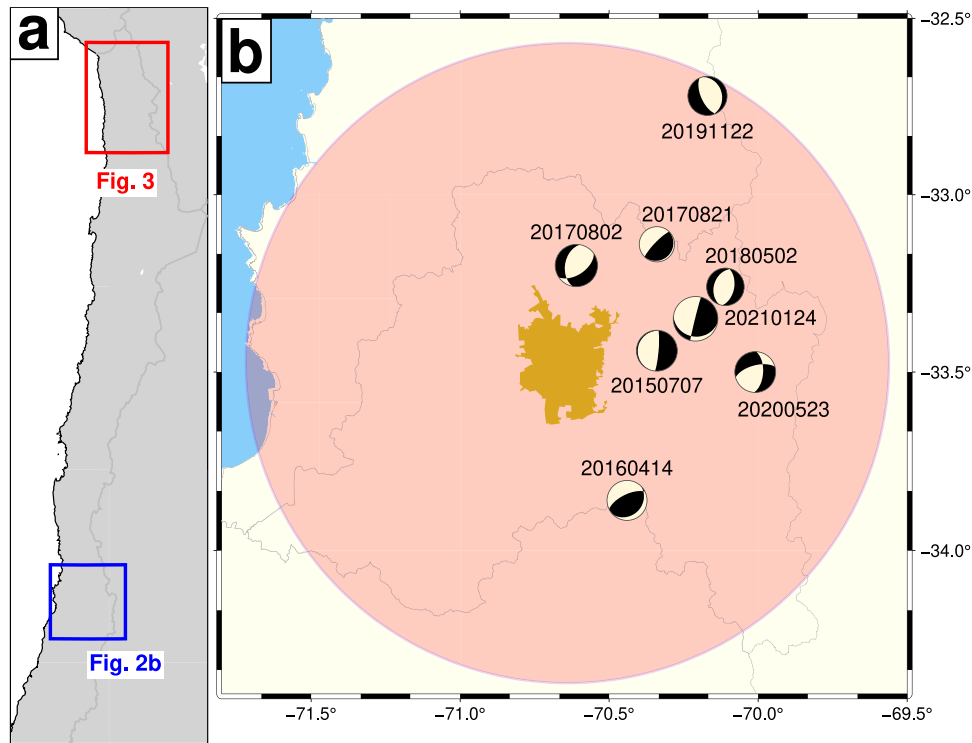


**Fig. 2.** (a) Location of the two study areas: Tarapacá (red square) and Santiago (blue square). (b) Epicentral location and focal mechanisms of the recent IID events (code = yyyyymmdd) below the metropolitan region considering depths between 97–122 km and magnitude between Mw 4.5–6 occurred in a perimeter of 100 km (pink shade) around the Santiago urban area (yellow area).

**Table 1**  
Seismic parameters of IID events. The first event listed corresponded to the 2005 Tarapacá earthquake in northern Chile. Then, we listed the moderate magnitude events occurred near Santiago from 2015 to 2021.

Date (yyyy/mm/dd)	Time (UTM)	Latitude	Longitude	Depth (km)	Magnitude (Mw)
2005/06/13	22:44:00	-19.98°	-69.19°	115	7.8
2015/07/07	13:35:14	-33.44°	-70.34°	117	5.2
2016/04/14	09:38:44	-33.86°	-70.44°	117	5.1
2017/08/02	07:15:13	-33.2°	-70.61°	99	5.4
2017/08/21	12:02:24	-33.14°	-70.34°	97	4.5
2018/05/02	16:09:54	-33.26°	-70.11°	110	4.8
2019/11/22	22:27:31	-32.72°	-70.17°	113	5
2020/05/23	13:11:00	-33.5°	-70.01°	118	5.2
2021/01/24	00:07:45	-33.35°	-70.21°	122	5.7

slip distribution of the 2005 Tarapacá earthquake proposed by [Delouis and Legrand \(2007\)](#), further details are provided in the following subsection.

### 3.3. Slip distribution model

An important parameter of the stochastic method related to the source properties is the slip model associated with each event. For large events ( $M > 7$ ), the characterization of a finite-fault model is recommended; however, for smaller events ( $M \sim 5$ ) recorded by regional stations, we assume a point source.

For the 2005 Tarapacá earthquake, the slip distribution determined using an inverse method by [Delouis and Legrand \(2007\)](#) was used, which considers 77 subfaults ( $11 \times 7$ ), with 10 km separations, and a maximum slip of 14.3 m (Fig. 3). Events with moderate magnitude (Table 2) are considered single faults or point faults, such as events 2017-08-02 (Mw 5.4) and 2021-01-24 (Mw 5.7), as described in Table 3. For scenarios A and B with Mw 7.8 IID earthquakes below Santiago, a slip distribution was used based on the slip distribution used for the 2005 Tarapacá earthquake, but its hypocenter (latitude,

longitude, depth), strike, dip, rake, and position of the subfaults ( $x$ ,  $y$ ) were changed by the parameters (values) of the IID events of moderate magnitude 2017-08-02 (Mw 5.4) and 2021-01-24 (Mw 5.7), respectively.

### 3.4. Selection of the parameters ( $Q_{0P}$ , $Q_{0S}$ , $\gamma$ , $\kappa_0$ , $\Delta\sigma$ ) used in the simulations

The other parameters are the quality factor constants for the P and S waves ( $Q_{0P}$  and  $Q_{0S}$ ), gamma ( $\gamma$ ), kappa ( $\kappa_0$ ), stress drop ( $\Delta\sigma$ ), soil type, and envelope function constants. These are inferred directly or from other studies such as  $Q_{0P}$  and  $Q_{0S}$  ([Otarola and Ruiz, 2016](#)),  $\kappa_0 = 0.025$  ([Neighbors et al., 2015; Pozo et al., 2023](#)),  $\gamma = 2.0$  ([Brune, 1970](#)), stress drop ([Peyrat et al., 2006; Herrera et al., 2023; Prieto et al., 2012](#)), and soil type ([Boore and Joyner, 1997; Leyton et al., 2011; Boore et al., 2011; Leyton et al., 2018a; Ojeda et al., 2021](#)). For other parameters for which there was no information for IID earthquakes, we considered the values introduced by [Ruiz et al. \(2018\)](#) as a reference and chose the best values by increasing or decreasing the original value by trial and error until we obtained synthetic records that best fit the observed records.

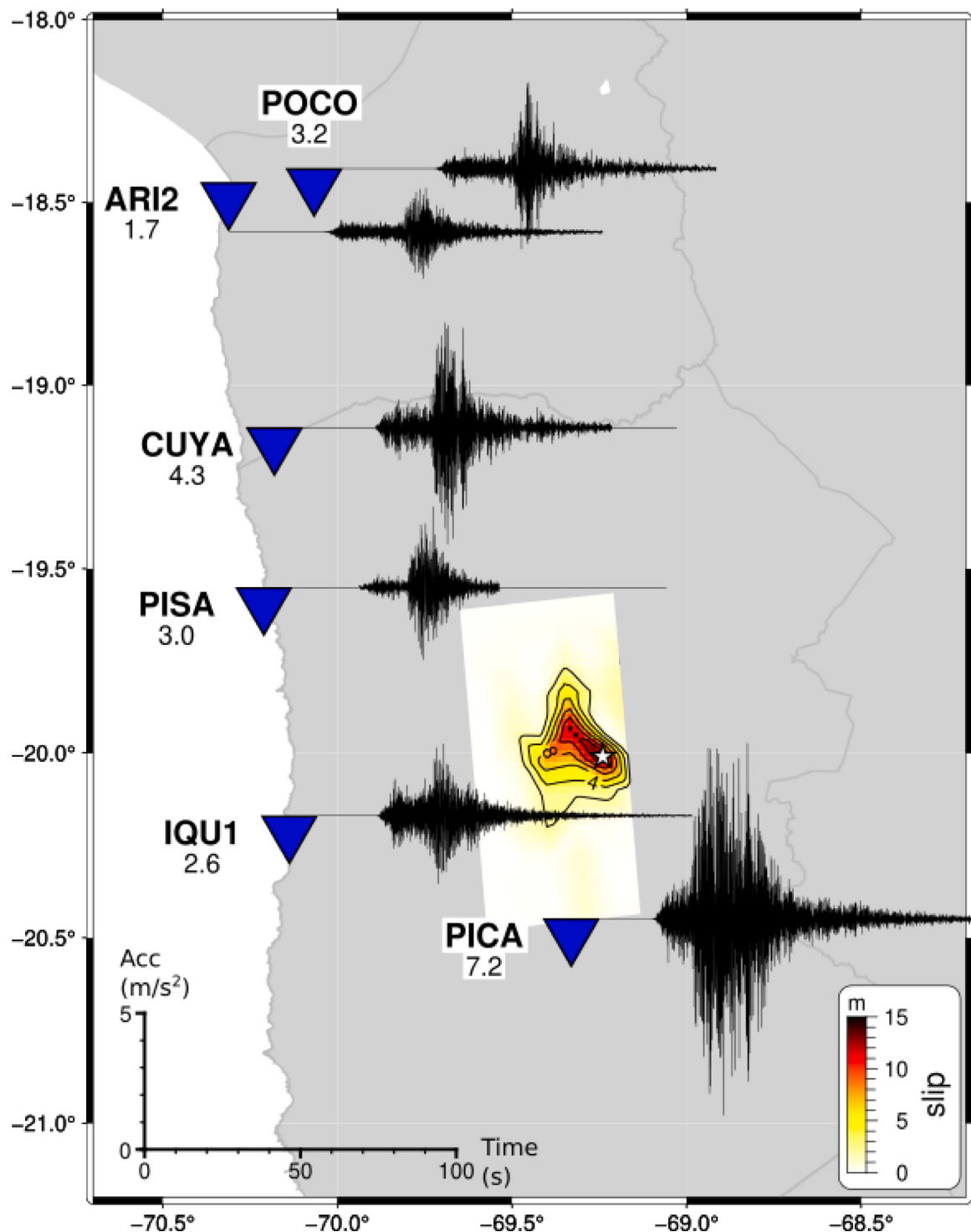


**Fig. 3.** Slip distribution for the 2005 Tarapacá earthquake from Delouis and Legrand (2007). The maximum slip value is 14.3 m. The map includes the epicenter (white star), seismic stations (blue inverted triangles), and EW component acceleration records (black accelerograms) with their PGA values next to each station.

An example is the estimation of the stress-drop values of moderate IID events. We used an average value of 200 bars as a reference, which has been obtained in other regions for moderate IID events (e.g., Prieto et al., 2012). The estimated stress drop values were between 120–495 bars, which are within the range of values estimated in other studies (Herrera et al., 2023; Kita and Katsumata, 2015; Prieto et al., 2012). The most important parameters for the 2017-08-02, 2021-01-24, and 2005 Tarapacá earthquakes are listed in Table 3.

## 4. Results

### 4.1. Moderate magnitude events

The moderate-magnitude events listed in Table 1 were simulated using a point fault for different soil conditions. For soil amplification, we used GRSA curves (Boore and Joyner, 1997; Ojeda et al., 2021), considering three soil types: Type A (rock), B (semi-consolidated),

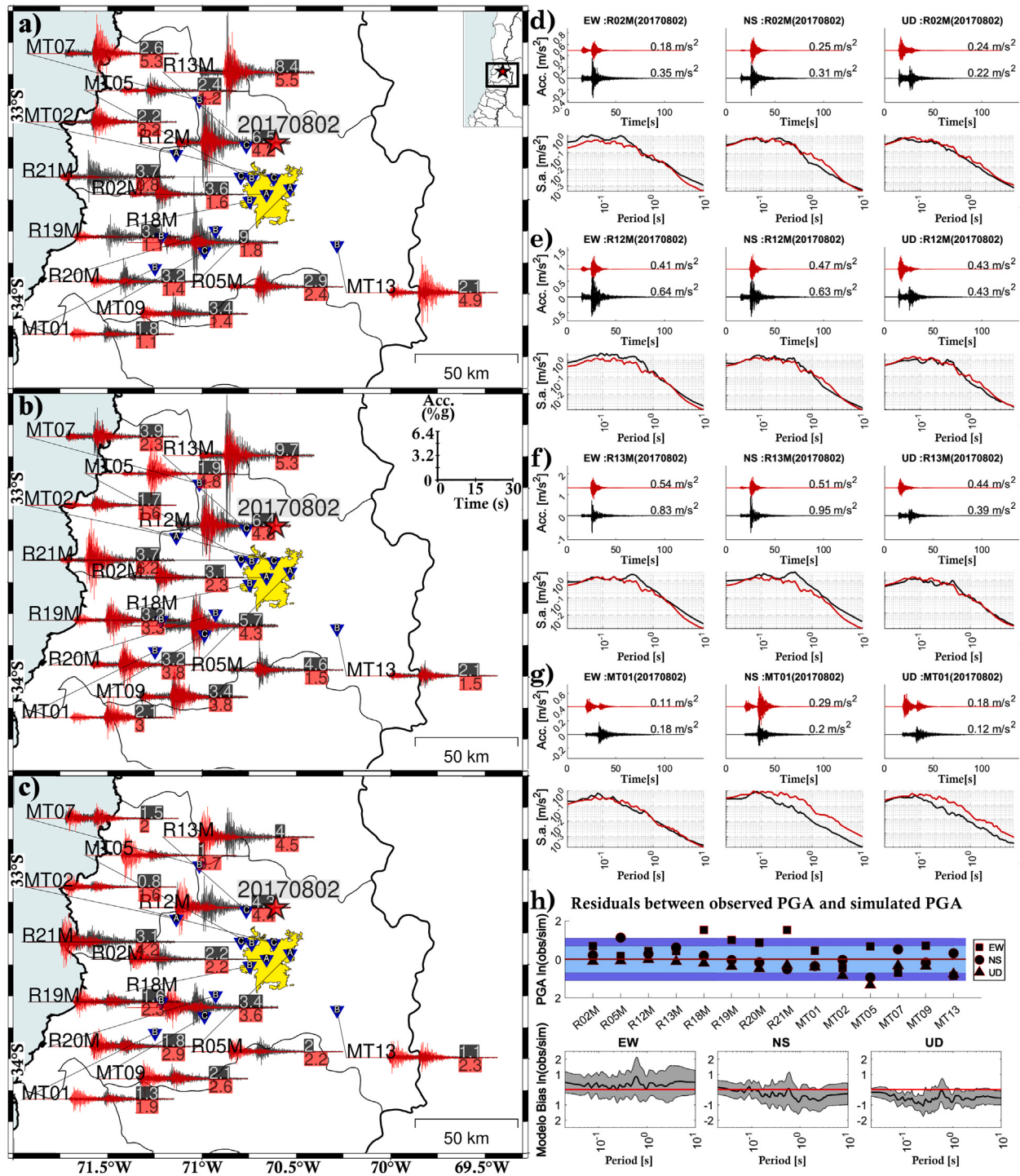


**Fig. 4.** Comparison of the observed (black) and simulated (red) acceleration records of the event 20170802, including their three components EW, NS, and Z in (a), (b), and (c), respectively, and the PGA values for the observed and simulated records at the end of each waveform. (d), (e), (f), and (j) Comparison of the records observed and simulated (top panel) and their response spectra (bottom panel) for the R02M, R12M, R13M, and MT02 stations, respectively. (h) Goodness-of-Fit (GOF) curve for all the simulated stations, the blue zone includes the values  $0.7 < |\ln(\text{obs}/\text{sim})| < 1.1$ , and the light blue zone highlights the values  $|\ln(\text{obs}/\text{sim})| < 0.7$ .

and C (low-consolidated). For the stations without Vs30 or VSz30, we chose the soil class that best fit the observed and synthetic records in all events; these results are indicated in Table 2. In this section, we present the simulation result for two events: 2017-08-02 of magnitude Mw 5.4 and 2021-01-24 of magnitude Mw 5.7. Table 3 shows the primary parameters used in the simulation. The results for the other events 2015-07-07, 2016-04-14, 2017-08-21, 2018-05-02, 2019-11-22,

and 2020-05-23 are attached in the Supplementary Material (see Fig. S1-S6).

Fig. 4 shows a comparison between the observed and synthetic records for the event 2017-08-02. In general, we observed a good fit in the time series except for seven records in the EW component, six of which are underestimated (R02M, R18M, R19M, R20M, R21M, and MT09), and one is overestimated (MT13) (Fig. 4a); also, in the NS

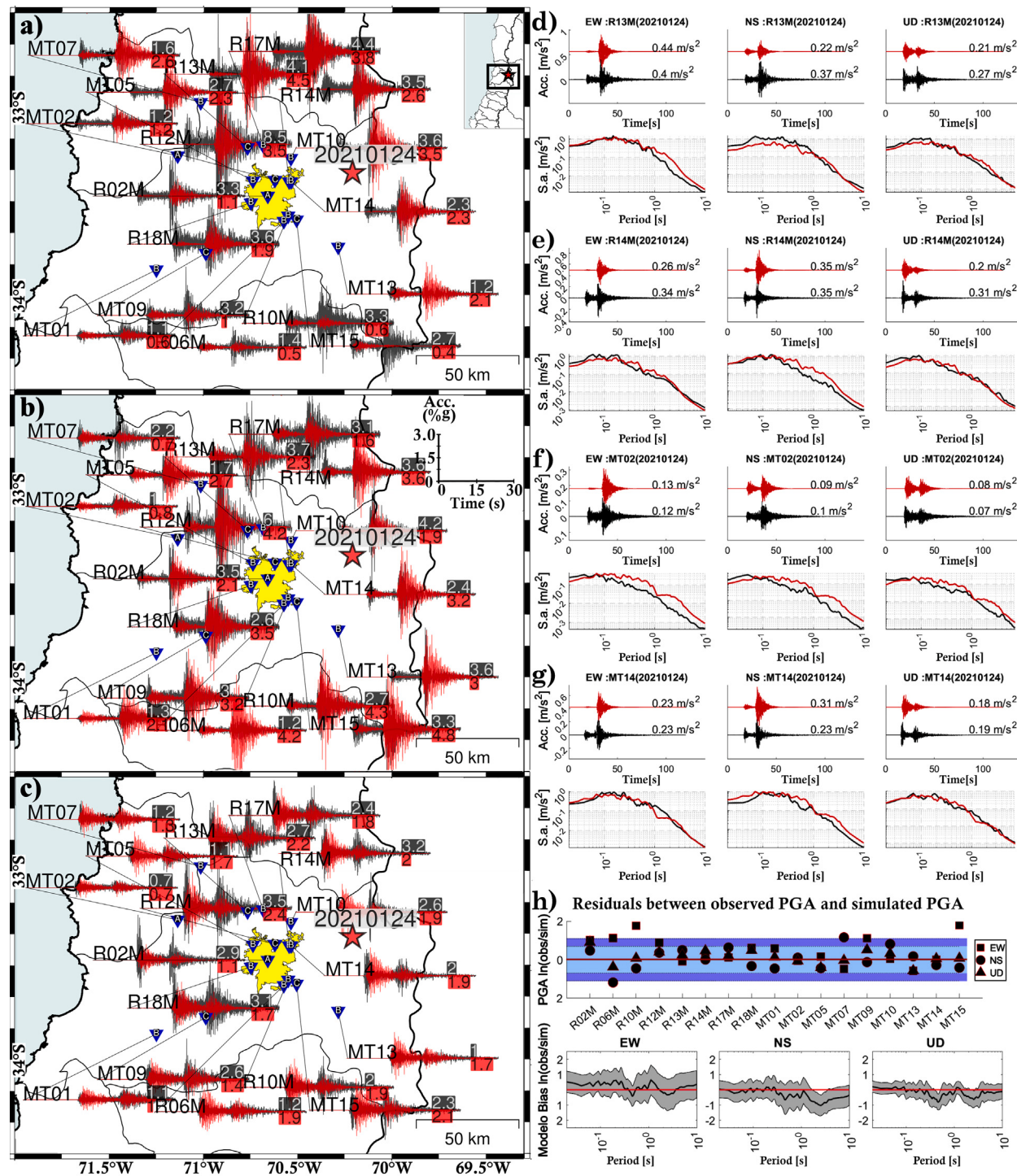


**Fig. 5.** Comparison of the observed (black) and simulated (red) acceleration records of the event 20210124, including their three components EW, NS, and Z in (a), (b), and (c), respectively, and the PGA values for the observed and simulated records at the end of each waveform. (d), (e), (f), and (j) Comparison of the records observed and simulated (top panel) and their response spectra (bottom panel) for the R13M, R14M, MT02, and MT14 stations, respectively. (h) Goodness-of-Fit (GOF) curve for all the simulated stations, the blue zone includes the values  $0.7 < |\ln(\text{obs}/\text{sim})| < 1.1$ , and the light blue zone highlights the values  $|\ln(\text{obs}/\text{sim})| < 0.7$ .

component, only one record is underestimated (R05M), and one other is overestimated (MT05) (Fig. 4b); besides, in the Z component, three records are overestimated (MT02, MT13, and MT05) (Fig. 4c). The goodness-of-fit curve (Graves and Pitarka, 2010) (Fig. 4h) showed a good fit ( $|\ln(\text{obs}/\text{sim})| < 0.7$ ) for 71.4% of the simulated records. We observed twelve records outside the range of good fit, eight of which had a high underestimation or overestimation with values between  $0.7 < |\ln(\text{obs}/\text{sim})| < 1.1$ , and the remaining four were severely

underestimated or overestimated compared to the observed records, reaching values of  $|\ln(\text{obs}/\text{sim})| > 1.1$ .

Fig. 5 compares the observed and synthetic records for the event of 2021-01-24. Here, we also observed a good fit except for six underestimated records in the EW component (R02M, R06M, R10M, R12M, MT09, and MT15) (Fig. 5a). In the NS component, we found discrepancies in two underestimated records (MT07 and MT10) and one overestimated record (R06M) (Fig. 5b). Finally, in the Z component,

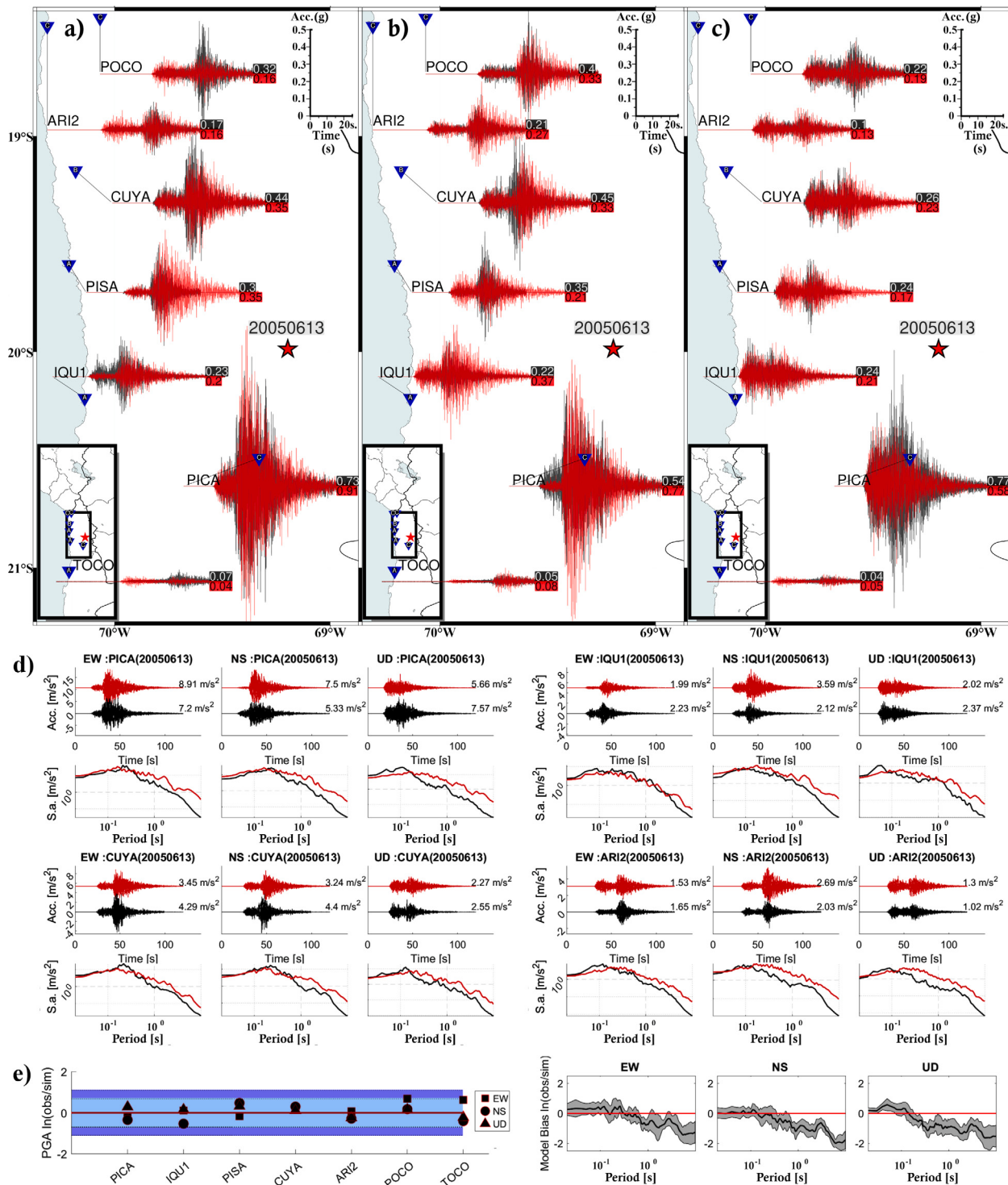


**Fig. 6.** Comparison of the observed (black) and simulated (red) acceleration records of its three components EW, NS, and Z in (a), (b), and (c), respectively, for the 2005 Tarapacá earthquake. The PGA values for the observed and simulated records are at the end of each waveform. (d) Comparison of the records observed and simulated for the PICA, IQUI, CUYA, and ARI2 stations (top panel) and their response spectra (bottom panel). (e) Goodness-of-Fit (GOF) curve for all simulated stations, the blue zone includes the values  $-0.7 < |\ln(\text{obs}/\text{sim})| < 1.1$ , and the light blue zone highlights the values  $|\ln(\text{obs}/\text{sim})| < 0.7$ .

only one record was underestimated (R02M) (Fig. 5c). The goodness-of-fit curve (Fig. 5h) showed a good fit ( $|\ln(\text{obs}/\text{sim})| < 0.7$ ) for 80.4% of the simulated records. We observed ten records outside the range of good fit; four of them have a high underestimation or overestimation with values between  $0.7 < |\ln(\text{obs}/\text{sim})| < 1.1$ , and the remaining six synthetic records are severely underestimated or overestimated with a value of  $|\ln(\text{obs}/\text{sim})| > 1.1$ .

#### 4.2. The 2005 Tarapacá Mw 7.8 earthquake

To corroborate the method for a large-magnitude event, we simulate the strong-ground motion records from the 2005 Tarapacá Mw 7.8 earthquake. A comparison of the observed and simulated records using the GRSA curves (Boore and Joyner, 1997; Ojeda et al., 2021) is presented in Fig. 6. Our results indicate a good fit in their waveform

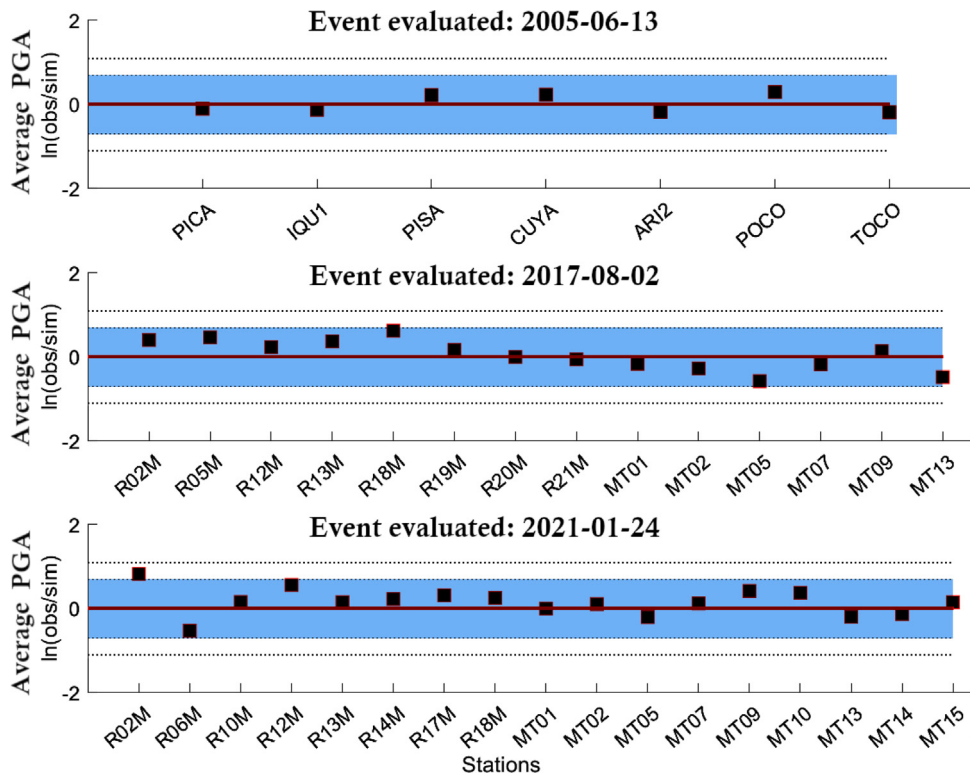


**Fig. 7.** Relationship between the observed and the simulated PGA average values for the 2005-06-13, 2017-08-02, and 2021-01-24 events. The light blue zone shows a bandwidth of  $|ln(obs/sim)| < 0.7$ .

**Table 2**

List of 23 stations located within a radius of 100 km from Santiago with at least one observed record simulated. The type of soil classification is listed for each station. VSz30 values are inferred from the CSN data and Pozo et al. (2023) (VSz30\*).

Station code	Longitude	Latitude	VSz30 (m/s)	Soil type code
R02M	-70.66°	-33.47°	1165	A
R05M	-70.53°	-33.44°	877	A
R06M	-70.57°	-33.61°	720	B
R07M	-70.69°	-33.37°	283	C
R10M	-70.55°	-33.58°	514	B
R12M	-70.62°	-33.39°	308	C
R13M	-70.77°	-33.22°	319	C
R14M	-70.55°	-33.4°	744	B
R17M	-70.68°	-33.21°	739	B
R18M	-70.75°	-33.51°	421	B
R19M	-71.22°	-33.7°	482	B
R20M	-70.93°	-33.67°	666	B
R21M	-70.8°	-33.38°	350	C
MT01	-71.25°	-33.86°	-	B
MT02	-71.14°	-33.26°	923*	A
MT03	-70.51°	-33.49°	-	C
MT05	-70.74°	-33.39°	496*	B
MT07	-71.02°	-32.98°	-	B
MT09	-70.99°	-33.78°	-	C
MT10	-70.54°	-33.27°	-	B
MT13	-70.29°	-33.74°	-	B
MT14	-70.54°	-33.4°	-	B
MT15	-70.51°	-33.6°	-	C

(duration and amplitude) and PGA values for all the stations in their three components. However, we observed a slight underestimation of the EW component at the POCO station. The goodness-of-fit curve (Fig. 6e) showed a good fit ( $|ln(obs/sim)| < 0.7$ ) in 95.2% of the simulated records, and only one simulation had a slight underestimate of the observed records with a value of  $|ln(obs/sim)| \sim 0.7$ . The analysis performed on the spectra using the goodness-of-fit method shows a

better fit in all three components in the frequency range of 0.25–14 Hz and period range of about 0.07–4 s (Fig. 6e).

To mitigate or eliminate the overestimations and underestimations of the results, a second analysis was performed between the observed and simulated PGAs, considering the average value of the PGA in its three components. Fig. 7 shows the relationship between the average PGA values of the real and synthetic strong-ground motion records. We observe that there is a better fit when considering station-by-station and component-by-component analyses. The percentage of records with a good fit ( $|ln(obs/sim)| < 0.7$ ) for 2005-06-13, 2017-08-02 and 2021-01-24 events are 100%, 100%, and 98%, respectively. These findings confirm that our simulations generally reproduced the strong-ground motion observed during IID earthquakes in northern Chile (2005-06-13) and near Santiago (2017-08-02 and 2021-01-24).

#### 4.3. Scenarios of possible intermediate-depth earthquakes (Mw 7.8) above Santiago

Eight scenarios were considered for a large earthquake below Santiago. Here, we present two scenarios (Fig. 8); the other six are shown in the Supplementary Material (see Fig. S7–S9) with the same moderated event code used as reference but with day “00”. The main parameters used for the scenarios were based on considerations from previous simulations. Two simulations were performed for 23 stations (Table 2) based on the parameters used to simulate the 2017-08-02 and 2021-01-24 events (Table 3). The main differences between these smaller magnitude events are the modification of their moment magnitude (Mw 7.8), stress drop (200 bars), and consideration of a finite fault model that replicates the slip distribution of the 2005 Tarapacá earthquake.

The first simulation (simulation A) considered parameters from the 2017-08-02 event. This simulation shows the largest PGA value of 1.03 g at the MT03 station (Z component). This value is directly related to soil classification (which is type C), the rupture distance (~100 km),

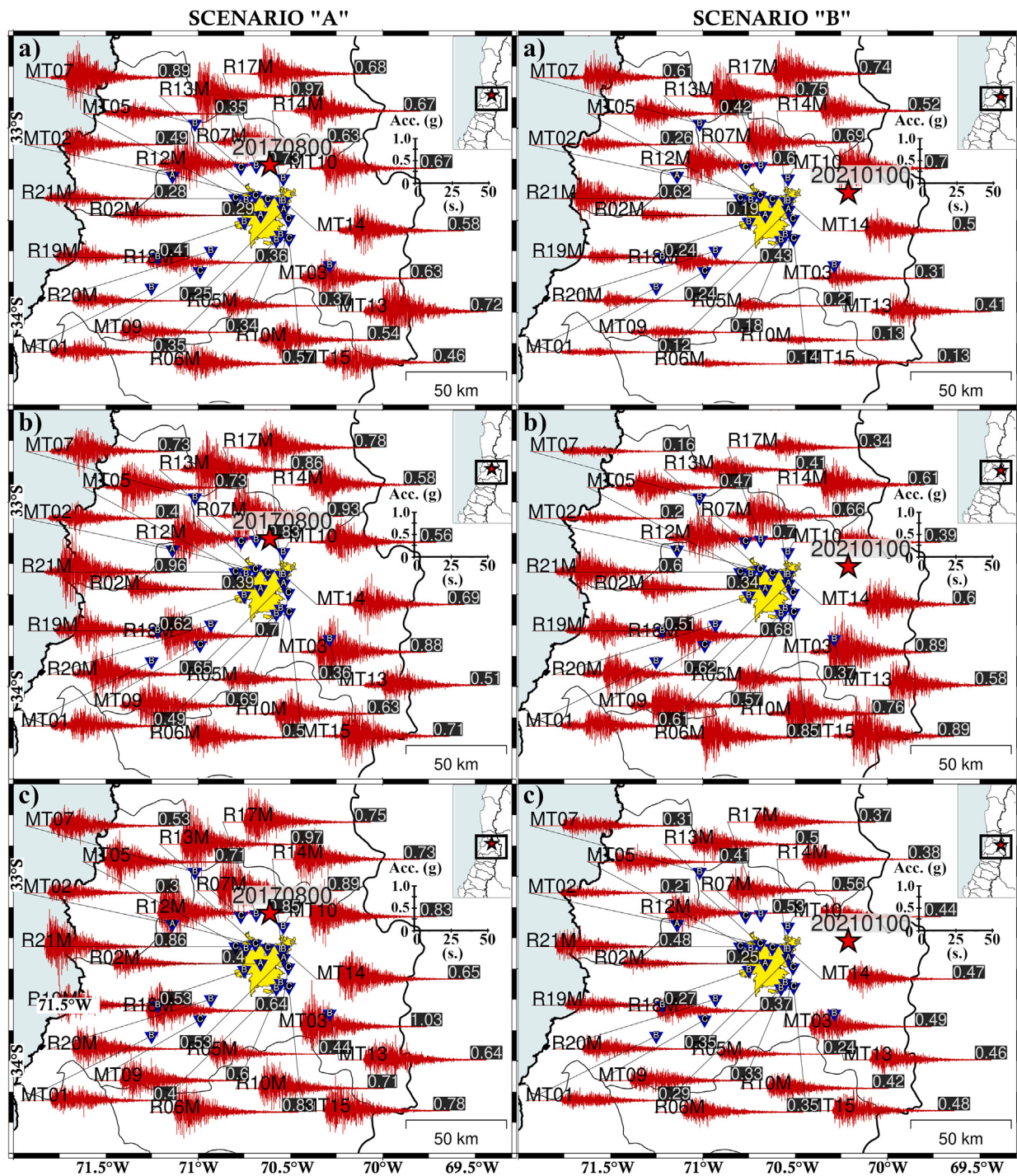


**Fig. 8.** Simulated acceleration records (red traces) for scenario A (Mw 7.8) with its EW, NS, and Z components in (a), (b), and (c), respectively (left panel). Simulated acceleration records (red traces) for scenario B (Mw 7.8) with its EW, NS, and Z components in (a), (b), and (c), respectively (right panel). The PGA values for the simulated records are shown at the end of each waveform.

the directivity effects and the takeoff angle. The next highest PGA value is 0.97 g at the R13M station (EW and Z components), and the smallest PGA value of 0.25 g at the R20M station (EW component). This dual behavior is directly related to soil classification, which are types C and B for the R13M and R20M stations, respectively. In addition, we considered a slight influence related to its rupture distances, which are 100 km and 116 km, respectively. Other high values were also observed in the EW component at station MT07 (0.89 g) and in the NS component at stations R21M (0.96 g) and R07M (0.93 g). The

PGA values at the remaining synthetic records are smaller than 0.89 g (Fig. 8a, b, and c).

The second simulation, hereafter simulation B, which considers the parameters for the 2021-01-24 event, shows the largest PGA value of 0.89 g at stations MT03 and MT15 (NS components) and the smallest PGA value of 0.12 g in the MT01 station (EW component). We primarily interpreted this behavior because of the difference in soil conditions (C for the MT03 and MT15 stations and B for the MT01 station) and rupture distances, which were 127 km, 129 km, and 177 km for the

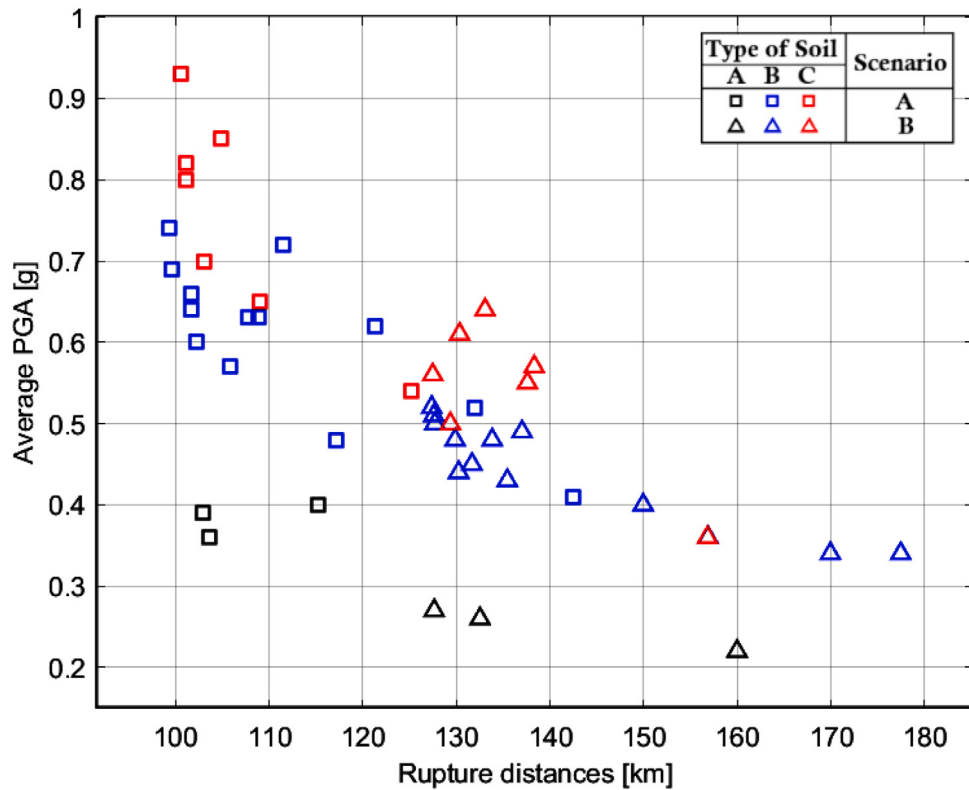


**Fig. 9.** Comparison of PGA average values regarding rupture distances in scenarios A (squares) and B (triangles). The colors black, blue, and red indicate the type of soil: A, B, and C, respectively.

**Table 3**

Seismic parameters used for the stochastic simulation of the 2017/08/02 (Mw 5.4), 2021/01/24 (Mw 5.7), and 2005/06/13 (Mw 7.8) events.

Parameters	2017-08-02 event	2021-01-24 event	2005-06-13 event	References
Date	2017/08/02	2021/01/24	2005/06/13	USGS
Origin time	07:15:13 UTM	00:07:45 UTM	22:44:33 UTM	USGS
Magnitude	Mw 5.4	Mw 5.7	Mw 7.8	USGS
Latitude, longitude	-33.2°, -70.61°	-33.35°, -70.21°	-19.98°, -69.19°	USGS
Depth	99 km	112 km	115 km	USGS
Source	Point source	Point source	Finite fault	This paper and Delouis and Legrand (2007)
Average slip	0.1 m	0.1 m	6.5 m	This paper
Strike, dip, rake	56°, 55°, -59°	194°, 88°, 69°	185°, 23°, -77°	USGS
Stress drop	390 bars	180 bars	200 bars	This paper
$V_p$ and $V_s$ at source	8.12 and 4.61 (km/s)	8.12 and 4.61 (km/s)	8.1 and 4.6 (km/s)	Campos et al. (2002) and Peyrat et al. (2006)
$Q_{0P}$ and $Q_{0S}$	1350 and 600	1350 and 600	1350 and 600	This paper
$\gamma$ and $\kappa_0$	2.0 and 0.025	2.0 and 0.025	2.0 and 0.025	This paper

MT03, MT15, and MT01 stations, respectively. Other high values were observed at stations R13M (EW component, 0.75 g), R06M (NS component, 0.85 g), and R10M (NS component, 0.76 g). The PGA values at the remaining synthetic records are smaller than 0.75 g (Fig. 8d, e, and f).

Only three high PGA values near ~1 g were obtained in simulation A (stations MT03, R13M and R21M, all with soil type C and rupture distances ~100 km). The rupture distances explain the difference between the PGA values obtained from scenarios A and B; while scenario B had stations located farther than 127 km, scenario A had 21 from 23 stations with rupture distances of less than 127 km.

The higher PGA values reproduced in these scenarios compared to the 2005 Tarapacá earthquake can be explained by the closeness between the stations and the source. For example, for the Tarapacá earthquake, the PICA station was the closest to the epicenter, and its rupture distance was 129.3 km. In contrast, for scenario A, only the R19M and MT01 stations have rupture distances greater than 130

km, which are 131.9 km and 142.5 km, respectively. The soil type is another factor that contributes significantly to the underestimation and overestimation of simulated records.

Fig. 9 shows the average PGA values for scenarios A and B. In general, we observe that the PGA values decrease as a function of distance and also the influence of soil type was clear: the low-consolidated soil (type C) had larger PGA values, and the lower PGA values were associated with rock soil (type A). However, dispersion can be associated with different parameters such as radiation patterns (takeoff and incident angles) and directivity effects. The average PGA values for the other six scenarios are shown in the Supplementary Material (see Fig. S10).

## 5. Conclusion

We simulated strong-ground motion records of IID events of moderate magnitude (Mw ~5–6) that occurred close to the Santiago metropolitan region using a stochastic method. Synthetic strong-ground motion

records generally reproduce the observed data well; their PGA average values are comparable, and the goodness-of-fit curve shows promising results. We reached a similar conclusion when comparing the synthetic strong-ground motion records with the real records for the 2005 Tarapacá Mw 7.8 earthquake, obtaining a good fit in their waveforms, amplitudes, and PGA values. Finally, the simulations of different scenarios of an Mw 7.8 earthquake occurring below Santiago show considerably strong-ground motion synthetic records with maximum PGA average values around 1.0 g. These maximum values occurred mainly due to a combination of two or more of the following four factors: the directivity effects, the takeoff angles, the minimum rupture distance (~100 km) and the soil C type, where the soil type factor is the most determinant of all. These results could be used in the future to create iso-acceleration maps (for multiple similar scenarios) and for seismic hazard studies in Santiago City. Finally, we emphasize the importance of understanding this type of earthquake that frequently occurs in subduction zones and that, as in the case of Chile, it can be very destructive, especially in the context of highly populated cities. Few studies have analyzed these IED earthquakes by employing a stochastic method (Kallas et al., 2018). Therefore, our results are particularly important and confirm that high-frequency, strong-ground motion simulations may be a good strategy. Further applications will allow us to extend these analyses to other subduction zones to re-evaluate the seismic hazards inferred from synthetic time histories.

#### CRediT authorship contribution statement

**Christian Flores:** Writing – original draft, Visualization, Validation, Software, Methodology, Investigation, Formal analysis, Conceptualization. **Javier Ojeda:** Writing – original draft, Software, Methodology. **Cristian Otarola:** Software, Methodology. **Sebastian Arriola:** Software, Methodology. **Sergio Ruiz:** Writing – original draft, Supervision, Data curation.

#### Declaration of competing interest

The authors declare that they have no known competing financial interests or personal relationships that could have appeared to influence the work reported in this paper.

#### Data availability

Data will be made available on request.

#### Acknowledgments

We thank the network and station operators of the Centro Sismológico Nacional (CSN, Chile) for their open access to the seismological and strong-motion data (<http://evtdb.csn.uchile.cl/>). We also thank the Red de Cobertura Nacional de Acelerógrafos (RENADIC) from the Universidad de Chile for making records of the 2005 Tarapacá earthquake still available (<http://terremotos.ing.uchile.cl/>). CF acknowledges support from the ANID scholarship ANID-PFCHA/Doctorado Nacional/2020-21200903, as well as to the Departamento de Geología and Departamento de Geofísica of the Universidad de Chile. SR thanks Agencia Nacional de Investigación y Desarrollo/Fondo Nacional de Desarrollo Científico y Tecnológico (ANID/FONDECYT; project no. 1200779). JO acknowledges support from the ANID scholarship ANID-PFCHA/Doctorado Nacional/2020-21200903. We thank the support from the Programa Riesgo Sísmico (PRS) of the Universidad de Chile. Finally, we thank the Editor of this special issue, E. Contreras-Reyes, and two anonymous reviewers for their thoughtful comments and suggestions that helped us to improve the original manuscript.

#### Appendix A. Supplementary data

Supplementary material related to this article can be found online at <https://doi.org/10.1016/j.jsames.2023.104501>.

#### References

- Aki, K., Richards, P.G., 2002. Quantitative seismology.
- Ammirati, J.-B., Vargas, G., Rebolledo, S., Abrahami, R., Potin, B., Leyton, F., Ruiz, S., 2019. The crustal seismicity of the western andean thrust (central Chile, 33°–34° S): Implications for regional tectonics and seismic hazard in the Santiago AreaThe crustal seismicity of the western andean thrust (central Chile, 33°–34° S). Bull. Seismol. Soc. Am. 109 (5), 1985–1999. <http://dx.doi.org/10.1785/0120190082>.
- Ammirati, J.-B., Villaseñor, A., Chevrot, S., Easton, G., Lehujer, M., Ruiz, S., Flores, M.C., 2022. Automated earthquake detection and local travel time tomography in the south-central andes (32–35° S): Implications for regional tectonics. J. Geophys. Res.: Solid Earth 127 (4), e2022JB024097. <http://dx.doi.org/10.1029/2022JB024097>.
- Barrantes, S., 2018. The seismic network of Chile. Seismol. Res. Lett. 89 (2A), 467–474. <http://dx.doi.org/10.1785/0220160195>.
- Beck, S., Barrantes, S., Kausel, E., Reyes, M., 1998. Source characteristics of historic earthquakes along the central Chile subduction Askew et Alzone. J. South Am. Earth Sci. 11 (2), 115–129. [http://dx.doi.org/10.1016/S0895-9811\(98\)00005-4](http://dx.doi.org/10.1016/S0895-9811(98)00005-4).
- Beresnev, I.A., Atkinson, G.M., 1997. Modeling finite-fault radiation from the  $\omega$  n spectrum. Bull. Seismol. Soc. Am. 87 (1), 67–84. <http://dx.doi.org/10.1785/BSSA070010067>.
- Bonnefoy-Claudet, S., Baize, S., Bonilla, L.F., Berge-Thierry, C., Pasten, C., Campos, J., Volant, P., Verdugo, R., 2009. Site effect evaluation in the basin of Santiago de Chile using ambient noise measurements. Geophys. J. Int. 176 (3), 925–937. <http://dx.doi.org/10.1111/j.1365-246X.2008.04020.x>.
- Boore, D.M., 1983. Stochastic simulation of high-frequency ground motions based on seismological models of the radiated spectra. Bull. Seismol. Soc. Am. 73 (6A), 1865–1894. <http://dx.doi.org/10.1785/BSSA07306A1865>.
- Boore, D.M., 2003. Simulation of ground motion using the stochastic method. Pure Appl. Geophys. 160, 635–676. <http://dx.doi.org/10.1007/PL00012553>.
- Boore, D.M., 2004. Estimating v s (30)(or NEHRP site classes) from shallow velocity models (depths < 30 m). Bull. Seismol. Soc. Am. 94 (2), 591–597. <http://dx.doi.org/10.1785/0120030105>.
- Boore, D.M., Joyner, W.B., 1997. Site amplifications for generic rock sites. Bull. Seismol. Soc. Am. 87 (2), 327–341. <http://dx.doi.org/10.1785/BSSA0870020327>.
- Boore, D.M., Thompson, E.M., Cadet, H., 2011. Regional correlations of VS 30 and velocities averaged over depths less than and greater than 30 meters. Bull. Seismol. Soc. Am. 101 (6), 3046–3059. <http://dx.doi.org/10.1785/0120110071>.
- Brune, J.N., 1970. Tectonic stress and the spectra of seismic shear waves from earthquakes. J. Geophys. Res. 75 (26), 4997–5009. <http://dx.doi.org/10.1029/JB075i026p04997>.
- Bustos, J., Pastén, C., Pavez, D., Acevedo, M., Ruiz, S., Astroza, R., 2023. Two-dimensional simulation of the seismic response of the Santiago Basin, Chile. Soil Dyn. Earthq. Eng. 164, 107569. <http://dx.doi.org/10.1016/j.soildyn.2022.107569>.
- Campos, J., Hatzfeld, D., Madariaga, R., López, G., Kausel, E., Zollo, A., Iannaccone, G., Fromm, R., Barrantes, S., Lyon-Caen, H., 2002. A seismological study of the 1835 seismic gap in south-central Chile. Phys. Earth Planet. Inter. 132 (1–3), 177–195. [http://dx.doi.org/10.1016/S0031-9201\(02\)00051-1](http://dx.doi.org/10.1016/S0031-9201(02)00051-1).
- Chen, Y., Wen, L., Ji, C., 2014. A cascading failure during the 24 May 2013 great Okhotsk deep earthquake. J. Geophys. Res.: Solid Earth 119 (4), 3035–3049. <http://dx.doi.org/10.1002/2013JB010926>.
- Cisternas, M., Torrejón, F., Gorigoitia, N., 2012. Amending and complicating Chile's seismic catalog with the Santiago earthquake of 7 August 1580. J. South Am. Earth Sci. 33 (1), 102–109. <http://dx.doi.org/10.1016/j.jsames.2011.09.002>.
- Delouis, B., Legrand, D., 2007. Mw 7.8 Tarapacá intermediate depth earthquake of 13 june 2005 (northern Chile): Fault plane identification and slip distribution by waveform inversion. Geophys. Res. Lett. 34 (1), <http://dx.doi.org/10.1029/2006GL028193>.
- Douglas, J., Aochi, H., 2008. A survey of techniques for predicting earthquake ground motions for engineering purposes. Surv. Geophys. 29, 187–220. <http://dx.doi.org/10.1007/s10712-008-9046-y>.
- González, F.A., Maksymowicz, A., Díaz, D., Villegas, L., Leiva, M., Blanco, B., Vera, E., Contreras, S., Cabrera, D., Bonvalot, S., 2018. Characterization of the depocenters and the basement structure, below the central Chile Andean Forearc: A 3D geophysical modelling in Santiago Basin area. Basin Res. 30 (4), 799–815. <http://dx.doi.org/10.1111/bre.12281>.
- Graves, R.W., Pitarka, A., 2010. Broadband ground-motion simulation using a hybrid approach. Bull. Seismol. Soc. Am. 100 (5A), 2095–2123. <http://dx.doi.org/10.1785/0120100057>.
- Green, H.W., Houston, H., 1995. The mechanics of deep earthquakes. Annu. Rev. Earth Planet. Sci. 23 (1), 169–213. <http://dx.doi.org/10.1146/annurev.ea.23.050195.001125>.

- Herrera, C., Pastén-Araya, F., Cabrera, L., Potin, B., Rivera, E., Ruiz, S., Madariaga, R., Contreras-Reyes, E., 2023. Rupture properties of the 2020 M  $w$  6.8 Calama (northern Chile) intraslab earthquake. Comparison with similar intraslab events in the region. *Geophys. J. Int.* 232 (3), 2070–2079. <http://dx.doi.org/10.1093/gji/gjac434>.
- Herrera, C., Ruiz, S., Madariaga, R., Poli, P., 2017. Dynamic inversion of the 2015 Jujuy earthquake and similarity with other intraslab events. *Geophys. J. Int.* 209 (2), 866–875. <http://dx.doi.org/10.1093/gji/ggx056>.
- Houston, H., 2015. *Treatise on geophysics*, volume 4: *Earthquake seismology*.
- Kita, S., Katsumata, K., 2015. Stress drops for intermediate-depth intraslab earthquakes beneath h okkaido, northern Japan: Differences between the subducting oceanic crust and mantle events. *Geochem. Geophys. Geosyst.* 16 (2), 552–562. <http://dx.doi.org/10.1002/2014GC005603>.
- Kkallas, C., Papazachos, C., Boore, D., Ventouzi, C., Margaris, B., 2018. Historical intermediate-depth earthquakes in the southern Aegean Sea Benioff zone: modeling their anomalous macroseismic patterns with stochastic ground-motion simulations. *Bull. Earthq. Eng.* 16, 5121–5150. <http://dx.doi.org/10.1007/s10518-018-0342-8>.
- Leyton, F., Leopold, A., Hurtado, G., Pastén, C., Ruiz, S., Montalva, G., Saéz, E., 2018b. Geophysical characterization of the chilean seismological stations: first results. *Seismological Research Letters* 89 (2A), 519–525. <http://dx.doi.org/10.1785/0220170156>.
- Leyton, F., Pastén, C., Ruiz, S., Idini, B., Rojas, F., 2018a. Empirical site classification of CSN network using strong-motion records. *Seismol. Res. Lett.* 89 (2A), 512–518. <http://dx.doi.org/10.1785/0220170167>.
- Leyton, F., Sepúlveda, S.A., Astroza, M., Rebolledo, S., Acevedo, P., Ruiz, S., González, L., Foncea, C., 2011. Seismic zonation of the Santiago basin, Chile. In: 5th International Conference on Earthquake Geotechnical Engineering.
- Magott, R., Fabbri, O., Fournier, M., 2016. Subduction zone intermediate-depth seismicity: Insights from the structural analysis of Alpine high-pressure ophiolite-hosted pseudotachylite (corsica, France). *J. Struct. Geol.* 87, 95–114. <http://dx.doi.org/10.1016/j.jsg.2016.04.002>.
- Motazedian, D., Atkinson, G.M., 2005. Stochastic finite-fault modeling based on a dynamic corner frequency. *Bull. Seismol. Soc. Am.* 95 (3), 995–1010. <http://dx.doi.org/10.1785/0120030207>.
- Neighbors, C., Liao, E., Cochran, E.S., Funning, G., Chung, A., Lawrence, J., Christensen, C., Miller, M., Belmonte, A., Andres Sepulveda, H., 2015. Investigation of the high-frequency attenuation parameter,  $\kappa$  (kappa), from aftershocks of the 2010 M  $w$  8.8 Maule, Chile earthquake. *Geophys. J. Int.* 200 (1), 200–215. <http://dx.doi.org/10.1093/gji/ggu390>.
- Ojeda, J., Akinci, A., Tinti, E., Arriola, S., Ruiz, S., 2021. Hybrid broadband strong-motion simulation to investigate the near-source characteristics of the M6. 5, 30 October 2016 Norcia, Italy earthquake. *Soil Dyn. Earthq. Eng.* 149, 106866. <http://dx.doi.org/10.1016/j.soildyn.2021.106866>.
- Otarola, C., Ruiz, S., 2016. Stochastic generation of accelerograms for subduction earthquakes. *Bull. Seismol. Soc. Am.* 106 (6), 2511–2520. <http://dx.doi.org/10.1785/0120150262>.
- Pastén, C., Sáez, M., Ruiz, S., Leyton, F., Salomón, J., Poli, P., 2016. Deep characterization of the Santiago Basin using HVSR and cross-correlation of ambient seismic noise. *Eng. Geol.* 201, 57–66. <http://dx.doi.org/10.1016/j.enggeo.2015.12.021>.
- Peyrat, S., Campos, J., de Chabalier, J.-B., Perez, A., Bonvalot, S., Bouin, M.-P., Legrand, D., Nercessian, A., Charade, O., Patau, G., et al., 2006. Tarapacá intermediate-depth earthquake (Mw 7.7, 2005, northern Chile): A slab-pull event with horizontal fault plane constrained from seismologic and geodetic observations. *Geophys. Res. Lett.* 33 (22), <http://dx.doi.org/10.1029/2006GL027710>.
- Pilz, M., Parolai, S., Stupazzini, M., Paolucci, R., Zschau, J., 2011. Modelling basin effects on earthquake ground motion in the Santiago de Chile basin by a spectral element code. *Geophys. J. Int.* 187 (2), 929–945. <http://dx.doi.org/10.1111/j.1365-246X.2011.05183.x>.
- Pozo, I., Montalva, G., Miller, M., 2023. Assessment of kappa values in the Chilean subduction zone for interface and in-slab events. *Seismo. Soc. Am.* 94 (1), 385–398. <http://dx.doi.org/10.1785/0220220018>.
- Prieto, G.A., Beroza, G.C., Barrett, S.A., López, G.A., Florez, M., 2012. Earthquake nests as natural laboratories for the study of intermediate-depth earthquake mechanics. *Tectonophysics* 570, 42–56. <http://dx.doi.org/10.1016/j.tecto.2012.07.019>.
- Ruiz, S., Ammirati, J.-B., Leyton, F., Cabrera, L., Potin, B., Madariaga, R., 2019. The January 2019 (M  $w$  6.7) Coquimbo earthquake: insights from a seismic sequence within the Nazca plate. *Seismol. Res. Lett.* 90 (5), 1836–1843. <http://dx.doi.org/10.1785/0220190079>.
- Ruiz, S., Madariaga, R., 2018. Historical and recent large megathrust earthquakes in Chile. *Tectonophysics* 733, 37–56. <http://dx.doi.org/10.1016/j.tecto.2018.01.015>.
- Ruiz, S., Ojeda, J., Pastén, C., Otarola, C., Silva, R., 2018. Stochastic strong-motion simulation in borehole and on surface for the 2011 Mw 9.0 tohoku-oki megathrust earthquake considering P, SV, and SH amplification transfer functions. *Bull. Seismol. Soc. Am.* 108 (5A), 2333–2346. <http://dx.doi.org/10.1785/0120170342>.
- Salomón, J., Pastén, C., Ruiz, S., Leyton, F., Sáez, M., Rauld, R., 2021. Shear wave velocity model of the Abanico Formation underlying the Santiago City metropolitan area, Chile, using ambient seismic noise tomography. *Geophys. J. Int.* 225 (2), 1222–1235. <http://dx.doi.org/10.1093/gji/ggaa600>.
- Saragoni, G.R., Hart, G.C., 1973. Simulation of artificial earthquakes. *Earthq. Eng. Struct. Dyn.* 2 (3), 249–267. <http://dx.doi.org/10.1002/eqe.4290020305>.
- Udías, A., Madariaga, R., Buforn, E., Muñoz, D., Ros, M., 2012. The large Chilean historical earthquakes of 1647, 1657, 1730, and 1751 from contemporary documents. *Bull. Seismol. Soc. Am.* 102 (4), 1639–1653. <http://dx.doi.org/10.1785/0120110289>.
- Vargas, G., Klinger, Y., Rockwell, T., Forman, S., Rebolledo, S., Baize, S., Lacassín, R., Armijo, R., 2014. Probing large intraplate earthquakes at the west flank of the Andes. *Geology* 42 (12), 1083–1086. <http://dx.doi.org/10.1130/G35741.1>.
- Wills, C., Petersen, M., Bryant, W., Reichle, M., Saucedo, G., Tan, S., Taylor, G., Treiman, J., 2000. A site-conditions map for California based on geology and shear-wave velocity. *Bull. Seismol. Soc. Am.* 90 (6B), S187–S208. <http://dx.doi.org/10.1785/0120000503>.
- Yáñez, G., Muñoz, M., Flores Aqueveque, V., Bosch, A., 2015. Gravity derived depth to basement in Santiago Basin, Chile: implications for its geological evolution, hydrogeology, low enthalpy geothermal, soil characterization and geo-hazards. <http://dx.doi.org/10.5027/andgeoV42n2-a01>.